Nanoscale

Accepted Manuscript

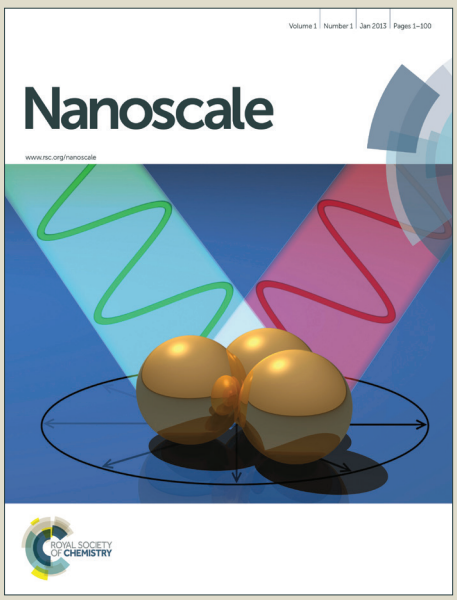

ROYAL SOCIETY OF CHEMISTRY

www.rsc.org/nanoscale

Cite this: DOI: 10.1039/c0xx00000x

www.rsc.org/xxxxxx

ARTICLE TYPE

$TiNb_2O_7$ Nanoparticles Assembled into Hierarchical Microspheres as High-Rate Capability and Long-Cycle-Life Anode Materials for Lithium Ion Batteries

Hongsen Li, Laifa Shen, Gang Pang, Shan Fang, Haifeng Luo, Kai Yang, and Xiaogang Zhang*

Received (in XXX, XXX) Xth XXXXXXXXX 20XX, Accepted Xth XXXXXXXXX 20XX
DOI: 10.1039/b000000x

As a competitor for $Li_4Ti_5O_{12}$ with a higher capacity and extreme safety, monoclinic $TiNb_2O_7$ has been considered as a promising anode material for next-generation high power lithium ion batteries. However, $TiNb_2O_7$ suffers from low electronic conductivity and ionic conductivity, which restricts the electrochemical kinetics. Herein, a facile and advanced architecture design of hierarchical $TiNb_2O_7$ microspheres is successfully developed for the large-scale preparation without any surfactant assistance. To the best of our knowledge, this is the first report on the on one step solvothermal synthesis of $TiNb_2O_7$ microspheres with micro- and nano-scale composite structures. When evaluated as anode materials for lithium-ion batteries, the electrode exhibits excellent high rate capacities and ultra-long cyclability, such as 258 mAh g^{-1} at 1 C, 175 mAh g^{-1} at 5 C, and 138 mAh g^{-1} at 10 C, extending to more than 500 cycles.

Rechargeable lithium ion batteries (LIBs) with high energy density and power density are essential for the replacement of internal combustion engine cars with electric vehicles, such as hybrid vehicles, plug-in hybrid vehicles and, ultimately, full electric vehicles.[1-8] For an anode material in LIB, the graphite are extensively spread as commercial anode materials because of their flat potential profile versus lithium and structural stability during cycling. However, graphite exhibits poor rate performance owing to their low lithium diffusion coefficient and presents serious safety issues because of potential solid electrolyte interphase (SEI) film formation which necessitates the determination of alternative negative electrodes.[9,10] Over the last decade, the titanium-based materials have been studied extensively as anode insertion hosts to reversibly accommodate Li-ions, for example, $Li_4Ti_5O_{12}$,[11-16] TiO_2,[17-19] TiP_2O_7[20], $LiCrTiO_4$[21] and $LiTi_2(PO_4)_3$.[22] However, the mentioned insertion-host materials showed low theoretical lithium charge capacity (< 200 mA h g^{-1}) with a Ti^{4+}/Ti^{3+} redox couple, resulting in a drastic reduction of overall energy density when coupled with a high performance cathode.[23,24] Therefore, it shows the great importance of the development of materials with large Li-ion storage capacities at high charge-discharge rates for the use as anodes in the LIBs of high power systems.

Recently, monoclinic $TiNb_2O_7$ has been considered as a promising anode material due to its high theoretical capacity of 387.6 mA h g^{-1} corresponded to 5 electron transfer reaction (Ti^{4+}/Ti^{3+}, Nb^{5+}/Nb^{3+}), ~2 times higher than $Li_4Ti_5O_{12}$. Furthermore, the operational voltage of $TiNb_2O_7$ is larger than 1.0 V (*vs*. Li/Li^+) which can effectively suppress the formation of an SEI layer, ensuring the safety and longer cycle life of the LIBs.[25-28] Despite these distinct advantages, $TiNb_2O_7$ still suffers from kinetic problems due to their intrinsic low electrical conductivity and slow solid-state diffusion of Li ions, resulting in the capacity fading and inferior high rate property.[29] As a consequence, the practical application of $TiNb_2O_7$ anode is limited. Following the first report of $TiNb_2O_7$ using the sol-gel techniques by Goodenough and coworkers,[28] several groups worldwide have articulated various processes for preparing nano-structured $TiNb_2O_7$ as LIB anodes. It has been widely acknowledged that nanosized electrode materials provide excellent rate capability by means of reducing lithium-ion diffusion distances and increasing the contact area between the active materials and the electrolyte.[30-33] However, a truly durable high rate capability for conversion electrode materials has rarely been achieved due to the electron transfer in the electrode is discontinuous. The reason is that owing to the structural anisotropy of the electrode, the electron transfer is strictly constrained at least in one dimension.[34,35] In this regard, a hierarchically porous three-dimensional electrode has attracted much attention. Despite the merits of the conventional nanostructured electrode, these hierarchically porous electrodes consist of different degrees of porosity with interconnective porous channels, which permit fine pentration of the electrolyte into the inner active materials and featured with fast charge transfer in three-dimensions. Up to now, the construction of hierarchical structures from well-crystalline $TiNb_2O_7$ nanoparticles has not been realized.

According to the previous studies, $TiNb_2O_7$ with rich porosity is usually fabricated with the assist of templates such as block copolymer,[24] F127[25] and SBA-15.[26] However, all the reported methods require a template or structure-directing agent, which increase the production cost and complexity. Herein, we reported a novel synthesis of hierarchical mircrospheres self-organized from $TiNb_2O_7$ nanoparticles without any surfactant assistance. To the best of our knowledge, it is the first report on one step

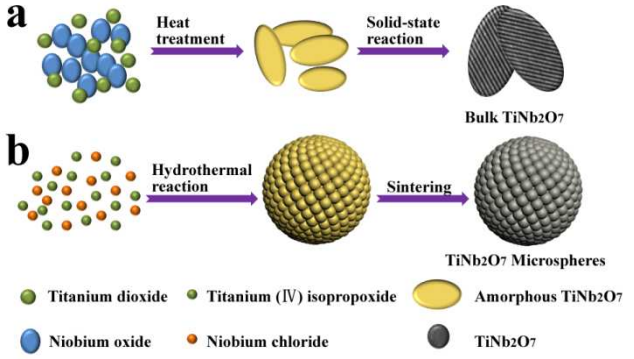

Scheme 1. Schematic comparison of growth process. (a) Conventional solid-state process for microsized bulk $TiNb_2O_7$. (b) Novel one step solvothermal synthesis of hierarchical $TiNb_2O_7$ microspheres.

solvothermal synthesis of hierarchical $TiNb_2O_7$ microspheres with micro- and nano-scale composite structures. With the advantages of the hierarchical porous structures consisting of numerous primary nanocrystallites, the $TiNb_2O_7$ microspheres exhibit exceptional high-rate capability and outstanding cyclic stability.

Scheme 1 illustrates the facile fabrication process leading to the powerful hierarchical $TiNb_2O_7$ microspheres architecture in comparison with the conventional solid-state method. For the solid-state procedure, the commercial titanium dioxide (TiO_2) and niobium oxide (Nb_2O_5) were employed. After sintering at a high temperature of 900 °C for 10 h, the microsized bulk $TiNb_2O_7$ were obtained. The representative morphology of the these samples which stacked by blocks and distributed inhomogeneous was shown in Fig. S1. While in our novel one step solvothermal synthesis process, we arrive at a homogeneous hierarchical $TiNb_2O_7$ microspheres composed of numerous nanosized primary nanoparticles (Fig. 1a). Here, the titanium (IV) isopropoxide ($C_{12}H_{28}O_4Ti$) and niobium chloride ($NbCl_5$) were chosen as the titanium and niobium precusors, respectively (a description of the detailed procedure can be found in the Experimental Section). The low synthesis temperature is another distinct merit compared with the conventional solid-state method and other reported methods for preparing $TiNb_2O_7$.[24-28] The high crystallinity and phase purity of the as-prepared $TiNb_2O_7$ mircrospheres were confirmed by X-ray diffraction (XRD) (Fig. 1b). All of the identified peaks can be perfectly indexed to monoclinic $TiNb_2O_7$ (space group: C2/m, JCPDS#: 39-1407). No other secondary or parasitic phase peaks, such as TiO_2, Nb_2O_5 and/or $Ti_2Nb_{10}O_{29}$ were detected,[36-38] which indicates the purity of the product. The pristine uncalcined $TiNb_2O_7$ microspheres were poorly crystalline, as shown in Fig. S2. Furthermore, the crystal structure of $TiNb_2O_7$ is demonstrated in Fig. 1c. The violet, green and red spheres represent niobium, titanium atoms and oxygen atoms, respectively. Fig. S3 shows the narrow-scan X-ray photoelectron spectroscopy (XPS) spectra of (a) Nb 3d, (b) Ti 2p in $TiNb_2O_7$ microspheres. An adventitious C1s peak at a binding energy of 284.5 eV was used to calibrate the obtained binding energy values. In Fig. S3, the $Nb3d_{3/2}$ (210.13 eV), $Nb3d_{5/2}$ (207.33 eV) and $Ti2p_{1/2}$ (464.33 eV), $Ti2p_{3/2}$ (458.88 eV) correspond to Nb^{5+} and Ti^{4+} in $TiNb_2O_7$, respectively.[25,38]

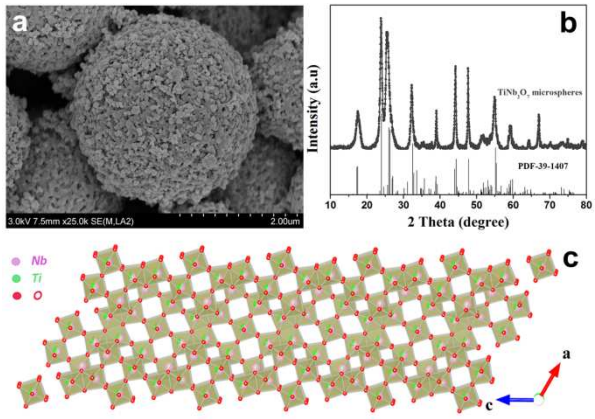

Fig. 1. (a) FESEM image and (b) XRD pattern of the as-synthesized $TiNb_2O_7$ microspheres. (c) The crystal structure of $TiNb_2O_7$, viewed along the b-axis.

The structure and morphology of the as-synthesized $TiNb_2O_7$ microspheres were characterized by field-emission scanning electron microscopy (FESEM) and transmission electron microscopy (TEM). Fig. 2a shows the panoramic morphologies of the sample, indicating that large-scale, monodisperse and uniform microspheres structures were obtained. It should be noted that the micro-structures are quite thermally stable without structural collapse. As shown from a higher magnification FESEM image in Fig. 2b and 2c, the as-obtained sample has a well-defined three-dimensional hierarchical architecture with diameters of 2~3 μm. Additionally, these microspheres are highly porous and composed of numerous highly uniform nanosized primary nanoparticles (Fig. 1a and Fig. 2c). In comparison, the $TiNb_2O_7$ samples obtained through different solvothermal time was shown in Fig. S4. On the basis of the SEM images, the author believes that the formation of $TiNb_2O_7$ microspheres is actually a process of nucleation of the primary $TiNb_2O_7$ nanoparticles following with self-organized growth procedures into microspheres, which is similar to the mechanism of the formation of $Li_4Ti_5O_{12}$ microspheres that has been reported.[39] A detailed crystallographic relationship between the $TiNb_2O_7$ microspheres and the nanoparticles was revealed by TEM, as shown in Fig. 2d-f. Fig. 2d is a typical low-magnification image of the $TiNb_2O_7$ microspheres, exhibiting the whole view of the three-dimensional hierarchical structure with diameter of about 2~3 μm, which is consistent with the observation of the FESEM images. The high-resolution transmission electron microscopy (HRTEM) image shown in Fig. 2f reveals the lattice fringes with interplane spacings of 0.34 nm, corresponding to the (-303) planes of monoclinic $TiNb_2O_7$ phase. Fig. 2h, 2i and 2j show the energy dispersive X-ray (EDX) elemental mappings for titanium, niobium and oxygen based on the area of the scanning transmission electron microscopy (STEM) image (Fig. 2g), respectively. The edge of titanium, niobium and oxygen EDX maps in Fig. 2h, 2i and 2j well match the result shown in the STEM image, indicating that titanium, niobium and oxygen are ultra-uniformly distributed throughout the microspheres. Moreover, the EDX spectrum of the $TiNb_2O_7$ microspheres were shown in Fig. S6, which shows strong Ti, Nb and O signals. The porosity feature of $TiNb_2O_7$ microspheres is examined by Brunauer-Emmett-Teller (BET) measurements shown in Fig. S5.

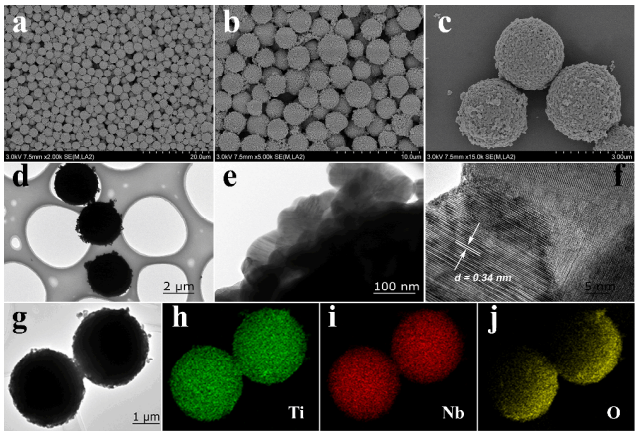

Fig. 2. (a, b, c) FESEM images and (d, e, f) TEM images of as-prepared $TiNb_2O_7$ microspheres. (g) STEM image of $TiNb_2O_7$. (h), (i) and (j) EDX elemental mapping of the area of (g), for titanium, niobium, and oxygen, respectively.

The BET surface area is calculated to be about 25.26 m^2 g^{-1} with a relatively narrow pore size distribution ranging from 2~48 nm. The corresponding Barrett-Joyner-Halenda (BJH) pore size distribution curve (Fig. S5b) shows that the pore size is not uniform, the maximum pore diameter and hierarchical distribution are 26.5 nm, 17.2 nm and 4.8 nm within the range of the mesopores (2~50 nm), which is consistent with the observation of FESEM and TEM. However, for the bulk $TiNb_2O_7$ samples, the BET surface area is only 5.21 m^2 g^{-1} which is much lower than the $TiNb_2O_7$ microspheres as shown in Fig. S5.

The electrochemical properties of $TiNb_2O_7$ microspheres were measured by configuring them as the laboratory-based CR2016 coin cell. $TiNb_2O_7$ microspheres as cathode was investigated versus Li metal under galvanostatic cycling conditions at room temperature in the voltage window of 1.0-3.0 V. Fig. 3a shows the first three cycles voltammograms of $TiNb_2O_7$ microspheres at a scanning rate of 0.1 mV s^{-1}. Apparently, the CV features in Fig. 3a were in general agreement with other nanostructured $TiNb_2O_7$ electrodes prepared by different methods reported in literatures.[24-26] One pair of sharp redox peaks were located at about 1.68 V and 1.62 V, which was attributed to the valence variation of Nb^{5+}/Nb^{4+}. Unlike the previous reported reference that there is one pair of shoulder peaks at about 1.50 and 1.56 V caused by different niobium states in $TiNb_2O_7$,[25,26] these redox peaks were not evident in $TiNb_2O_7$ microspheres. The broad bump in the range of 1.0-1.4 V may correspond to the Nb^{4+}/Nb^{3+} redox couples. In addition to the above mentioned peaks, another pair of cathodic/anodic peaks at about 1.73 and 2.0 V could be regarded as the redox reactions of Ti^{4+}/Ti^{3+}. Note that all curves almost overlap, suggesting super cyclability and fine kinetics at the electrode. The electrochemical behavior of the $TiNb_2O_7$ microspheres was further studied under galvanostatic conditions. As displayed in Fig. 3b, the voltage profiles present sloping lines during both charge and discharge processes, in accordance with the broad peaks observed in CV curves. The initial lithiation (discharge) capacity of the $TiNb_2O_7$ microspheres was 351.7 mAh g^{-1} as shown in Fig. 3b. A safe voltage range (1.0-3.0 V) was set with the aim to protect the electrodes from SEI formation.

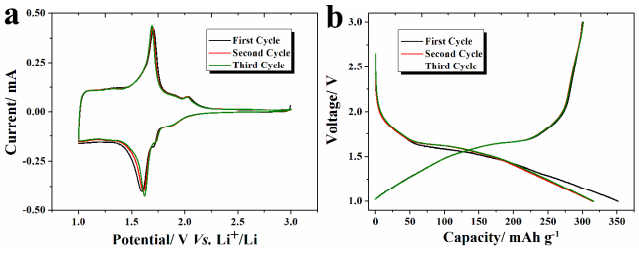

Fig. 3. (a) Cyclic voltammograms curves of $TiNb_2O_7$ microspheres at a scanning rate of 0.1 mV s^{-1}, (b) the charge/discharge curves of $TiNb_2O_7$ microspheres at the rate of 0.1 C.

In the following 2nd and 3rd cycles, a stable discharge capacity of about 316 mAh g^{-1} was achieved, which is 81.6% compared to their theoretical capacity.

To evaluate the rate performance of the $TiNb_2O_7$ microspheres, the electrodes were conducted using the multiple-current galvanostatical testing. The $TiNb_2O_7$ microspheres were tested at the C-rate of 0.5, 1, 2, 5, 10 and 20 C, calculated from the theoretic capacity of $TiNb_2O_7$ (namely, approximate to the currents of 0.1935, 0.387, 0.774, 1.935, 3.87 and 7.74 A g^{-1} respectively), and then returned 1 C step by step (10 cycles per step). The discharge curves of first cycle of each step are summarized in Fig. 4a (except that the second cycle is selected at 0.5 C). It is apparent that the discharge curves of $TiNb_2O_7$ microspheres at low rates present two sloping regions (above 1.7 V and below 1.6 V) and a plateau (about 1.65 V) reflecting the Li^+ insertion behavior. With increasing current rate, the distinguish between the two discharge plateaus gradually becomes blurred and the plateau voltages shift toward lower potentials because of the increased cell polarization at high current rates.[40,41] The discharge capacity of $TiNb_2O_7$ microspheres can be as high as 258 mAh g^{-1} at 1 C rate, and the capacity is still retained at ~100 mAh g^{-1} even at the very high rate of 20 C, indicating the excellent rate capability. In comparison, the bulk $TiNb_2O_7$ was tested using the same method as shown in Fig. 4b. Obviously, the discharge capacity of bulk $TiNb_2O_7$ electrodes was dramatically faded with the values of 138.1 mAh g^{-1} at 1 C, and only 36.6 mAh g^{-1} at 10 C. The electrochemical performance of multiple-current testing is shown in Fig. 4c. It is clear that the $TiNb_2O_7$ microspheres electrode exhibits extreme high capacity and excellent cycling property during high rate testing. Furthermore, when the current density backed to 1 C, the discharge capacity of the $TiNb_2O_7$ microspheres electrode was recovered to the 256 mAh g^{-1} which was nearly the same as the previous measurement. In contrast, after high rate cycling, the capacity of bulk $TiNb_2O_7$ cannot recover to initial levels even at low discharge currents (Fig. S7). Fig. 4d shows the cycling performance of $TiNb_2O_7$ microspheres at current rate of 10 C. Apparently, the $TiNb_2O_7$ microspheres shows good cyclic capacity retention with a high reversible capacity of about 115.2 mAh g^{-1} retained after 500 cycles. In order to further understand the enhanced lithium storage properties of these monoclinic $TiNb_2O_7$ microspheres, we carried out post-mortem studies after 100 charge discharge cycles at 5 C. As shown in Fig. S8, the overall hierarchical spheres structures

can be good retained, which suggests that the $TiNb_2O_7$ microspheres are robust enough to endure the large current

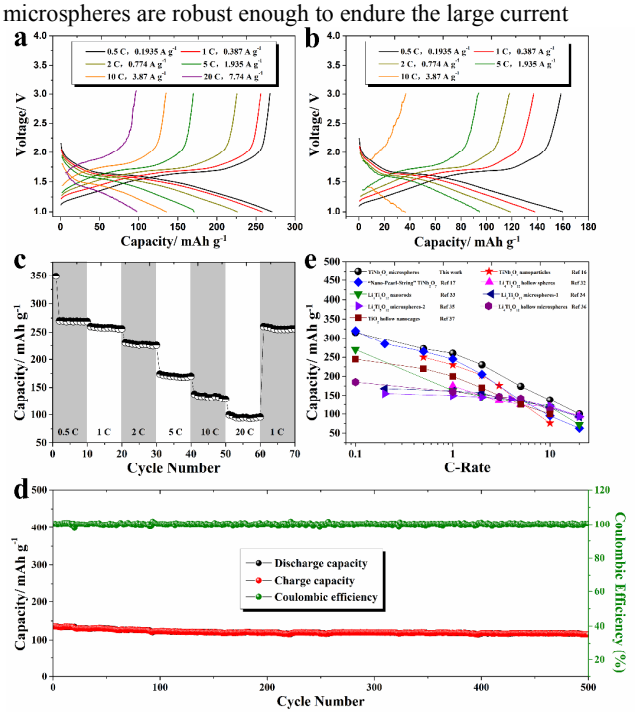

Fig. 4. The voltage profiles of (a) the $TiNb_2O_7$ microspheres electrode and (b) pure $TiNb_2O_7$ cycled at various rates; (c) The multi-rate testing at the discharge currents of 0.5, 1, 2, 5, 10, 20, and 1 C, respectively. (d) Cycling performances of $TiNb_2O_7$ microspheres at the rate of 10 C. (e) Comparison of rate capability of $TiNb_2O_7$ microspheres with other Ti-based high rate electrodes reported recently.

charge/discharge process and explains the ultra-long life properties of the batteries assembled. We also compared the current work with other Ti-based high rate electrodes reported in the recent research literature, including $TiNb_2O_7$ nanoparticles,[26] "Nano-Pearl-String" $TiNb_2O_7$,[27] $Li_4Ti_5O_{12}$ hollow spheres,[42] $Li_4Ti_5O_{12}$ nanorods,[43] $Li_4Ti_5O_{12}$ microspheres,[39,44] $Li_4Ti_5O_{12}$ hollow microspheres,[45] TiO_2 hollow nanocages,[46] and these results are shown in Fig. 4e. By comparison, the $TiNb_2O_7$ microspheres electrode exhibits higher specific capacities and outstanding rate performance under different current densities.

In summary, we have designed a novle route to synthesize the $TiNb_2O_7$ microspheres via a facile solvothermal methode without any templates. These hierarchical spheres self-assembled from well-crystalline $TiNb_2O_7$ nanoparticles with a three-dimensional nanoporous structure exhibit high specific capacities, exceptionally high rate performance and ultra-long cyclic stability, when used as anode materials in Li ion batteries. We conclude that the excellent electrochemical performance originates from the uniform distribution of the primary $TiNb_2O_7$ nanoparticles in the hierarchical spheres which can provide extra active position for Li^+ storage, and effectively shorten the pathway for Li^+ diffusion; on the other hand, the porous $TiNb_2O_7$ electrodes consist of different degrees of porosity with interconnective porous channels affords an extremely effective three-dimensional network for fast electron transport. These results indicated their great potential application as promising candidates for the development of high-performance, advanced lithium batteries directed to the hybrid vehicles, plug-in hybrid vehicles and full electric vehicles.

Experimental Section

Materials synthesis: In a typical procedure, 0.27 g niobium chloride ($NbCl_5$; 99.99%, Aladdin) was added to 22 mL of ethanol. After the solution was gently stirred for a few minutes, 0.142 g of titanium (IV) isopropoxide ($C_{12}H_{28}O_4Ti$, TIP; 97%, Aladdin) was added. The reaction solution was then transferred to a 30 mL Teflon-lined stainless steel autoclave and kept in an electric oven at 200 °C for different times. The autoclave was then taken out of the oven and left to cool naturally to room temperature. The white precipitate was separated by centrifugation, washed several times with deionized water and ethanol and dried at 80 °C overnight. All of the products were calcined at 700 °C for 2 h with a heating rate of 3 °C min^{-1} to obtain a highly crystalline monoclinic phase. For comparison, pure $TiNb_2O_7$ were synthesized via a solid state reaction route. In brief, 1.329 g niobium oxide (Nb_2O_5), 0.3995 g titanium dioxide (TiO_2) and zirconia balls were mixed in alcohol and stirred by a planetary mill at a speed of 400 rpm for 2 h. Finally, the resulting slurry was dried and furthered calcined at 900 °C for 10 h.

Materials characterization: The crystal structure of the obtained samples was characterized by X-ray diffraction (XRD) (Bruker D8 advance) with Cu Ka radiation. Microstructural properties were determined using transmission electron microscopy (TEM) (TEM, FEI, Tecnai-20), high-resolution transmission electron microscopy (HRTEM, JEOL JEM-2010), and field-emission scanning electron microscopy (FESEM, HITACHI S-4800). The N_2 adsorption/desorption were determined by Brunauer-Emmett-Teller (BET) measurements using an ASAP-2010 surface area analyzer. The X-ray photoelectron spectroscopy (XPS) analysis was performed on a Perkin-Elmer PHI 550 spectrometer with Al Kα (1486.6 eV) as the X-ray source.

Electrochemical Measurement: Electrochemical evaluations were performed by galvanostatic cycling in a CR2016-type coin cell. The working electrodes were formed by mixing 75 wt.% active materials, 15 wt.% carbon black, and 10 wt.% polyvinylidene fluoride dissolved in N-methyl pyrrolidinone, and pasting the mixture on a copper-foil current collector. Afterwards, the electrode was dried under vacuum at 110 °C for 12 h. The cells were assembled with the cathode as prepared, lithium metal as anode and polypropylene (PP) film as separator. The electrolytes were 1 mol L^{-1} $LiPF_6$ solution in a 1 : 1 (V : V) mixture of ethylene carbonate (EC) and dimethyl carbonate (DMC). All the Test cells assembly process was in an argon-filled glove box. Galvanostatically charge-discharge experiments were performed at different current densities between 1.0 and 3.0 V (vs. Li/Li^+) using a CT2001A cell test instrument (LAND Electronic Co.). Cyclic voltammetry (CV) studies were carried out on an electrochemical workstation (CH Instruments, model 660C)

Acknowledgements

This work is financially supported by the National Program on Key Basic Research Project of China (973 Program, No. 2014CB239701), National Natural Science Foundation of China (No. 21173120, 51372116), Natural Science Foundations of Jiangsu Province (No.BK2011030), Fundamental Research Funds for the Central Universities of NUAA (NP2014403), Funding for Outstanding Doctoral Dissertation in NUAA (BCXJ14-10), Funding of Jiangsu Innovation Program for Graduate Education (KYLX_0255) and the Fundamental Research Funds for the Central Universities.

Notes and references

College of Materials Science and Engineering, Jiangsu Key Laboratory of Material and Technology for Energy Conversion, Nanjing University of Aeronautics and Astronautics, 29 Yudao road, Nanjing, 210016, P. R. China. Email: azhangxg@nuaa.edu.cn

† Electronic Supplementary Information (ESI) available: [SEM, BET and electrochemical data of the bulk $TiNb_2O_7$, XRD pattern of the uncalcined $TiNb_2O_7$ microspheres, additional XPS, SEM, BET and EDX data for $TiNb_2O_7$ microspheres.]. See DOI:10.1039/b000000x/

1 H. G. Jung, M. W. Jang, J. Hassoun, Y-K, Sun, B. Scrosati, *Nat. Commun.,* 2011, **2**, 1.
2 M. Pharr, K. J. Zhao, X. W. Wang, Z. G. Suo, J. J. Vlassak, *Nano Lett.*, 2012, **12**, 5039.
3 X. L. Wu, L. Y. Jiang, F. F. Cao, Y. G. Guo, L. J. Wan, *Adv. Mater.,* 2009, **21**, 2710.
4 Y. Yu, C. L. Yan, L. Gu, X. Y. Lang, K. Tang, L. Zhang, Y. Hou, Z. F. Wang, M. W. Chen, O. G. Schmidt, J. Maier, *Adv. Energy Mater.,* 2013, **3**, 281.
5 Y. J. Gong, S. B. Yang, L. Zhan, L. L. Ma, R. Vajtai, P. M. Ajayan, *Adv. Funct. Mater.* 2014, DOI: 10.1002/adfm.201300844.
6 K. J. Zhao, M. Pharr, L. Hartle, J. J. Vlassak, Z. G. Suo, *J. Power Sources*, 2012, **218**, 6.
7 G. Y. Zheng, Y. Yang, J. J. Cha, S. S. Hong, Y. Cui, *Nano Lett*., 2011, **11**, 4462.
8 J. Wang, Y. Yu, L. Gu, C. L. Wang, K. Tang, J. Maier, *Nanoscale,* 2013, **5***,* 2647.
9 H. S. Li, L. F. Shen, X. G. Zhang, J. Wang, P. Nie, Q. Che, B. Ding, *J. Power Sources,* 2013, **221**, 122.
10 O. Crowther, A. C. West, *J. Electrochem. Soc.,* 2008, **155,** A806.
11 Y. B. Shen, Eltzholtz, B. B. Iversen, *Chem. Mater.,* 2013, **25**, 5023.
12 H. S. Li, L. F. Shen, J. Wang, B. Ding, P. Nie, G. Y. Xu, X. Y. Wang, and X. G. Zhang, *ChemPlusChem*, 2014, **79**, 128.
13 J. Lu, K. P. Song, P. A. V. Aken, J. Maier, Y. Yu, *Nano Lett.,* 2014, **14**, 2597.
14 J. M. Feckl, K. Fominykh, M. Döblinger, D. Fattakhova-Rohlfing, T. Bein, *Angew. Chem. Int. Ed.,* 2012, **51**, 7459.
15 L. F. Shen, H. S. Li, E. Uchaker, X. G. Zhang, G. Z. Cao, *Nano Lett.,* 2012, **12**, 5673.
16 A. Laumann, M. Bremholm, P. Hald, M. Holzapfel, K. T. Fehr, B. B. Iversen, *J. Electrochem. Soc.,* 2012, **159**, A166.
17 Z. Q. Wang, X. Li, H. Xu, Y. Yang, Y. J. Cui, H. G. Pan, Z. Y. Wang, B. L. Chen, G. D. Qian, *J. Mater. Chem. A,* 2014, DOI: 10.1039/C4TA02029D.
18 Z. G. Lu, C. T. Yip, L. P. Wang, H. T. Huang, L. M. Zhou, *ChemPlusChem,* 2012, **77**, 991.
19 D. H. Wang, D. W. Choi, J. Li, Z. G. Yang, Z. M. Nie, R. Kou, D. H. Hu, C. M. Wang, L. V. Saraf, J. G. Zhang, I. A. Aksay, J. Liu, *ACS Nano,* 2009, **3**, 907.
20 S. Patoux, C. Masquelier, *Chem. Mater.,* 2002, **14**, 5057.
21 V. Aravindan, W. Chuiling, S. Madhavi, *J. Mater. Chem*., 2012, **22**, 16026.
22 V. Aravindan, W. Chuiling, M. V. Reddy, G. V. S. Rao, B. V. R. Chowdari, S. Madhavi, *Phys. Chem. Chem. Phys*., 2012, **14**, 5808.
23 R. Satish, V. Aravindan, W. C. Ling, J. B. Goodenough, S. Madhavi, *Adv. Energy Mater*., 2014, DOI: 10.1002/aenm.201301715.
24 C. Jo, Y. Kim, J. Hwang, J. Shim, J. Chun, J. Lee, *Chem. Mater.,* 2014, DOI:10.1021/cm501011d.
25 B. K. Guo, X. Q. Yu, X. G. Sun, M. F. Chi, Z. A. Qiao, J. Liu, Y. S. Hu, X. Q. Yang, J. B. Goodenough, S. Dai, *Energ. Environ. Sci.,* 2014, DOI: 10.1039/C4EE00508B.
26 L. Fei, Y. Xu, X. F. Wu, Y. L. Li, P. Xie, S. G. Deng, S. Smirnovc, H. M. Luo, *Nanoscale*, 2013, **5**, 11102.
27 K. Tang, X. K. Mu, P. A. V. Aken, Y. Yu, J. Maier, *Adv. Energy Mater*., 2013, **3**, 49.
28 J-T. Han, Y-H. Huang, J. B. Goodenough, *Chem. Mater*., 2011, **23**, 2027.
29 P. L. Taberna, S. Mitra, P. Poizot, P. Simon, J. M. Tarascon, *Nat. Mater*., 2006, **5**, 567.
30 Z. Y. Wang, L. Zhou, X. W. Lou, *Adv. Mater*., 2012, **24**, 903.
31 H. S. Li, L. F. Shen, K. B. Yin, J. Ji, J. Wang, X. Y. Wang, X. G. Zhang, *J. Mater. Chem. A,* 2013, **1**, 7270.
32 A. S. Aricó, P. Bruce, B. Scrosati, J. M. Tarascon, W. V. Schalkwijk, *Nat. Mater.,* 2005, **4**, 366.
33 H. Jiang, P. S. Lee, C. Z. Li, *Energy Environ. Sci*., 2013, **6**, 41.
34 X. Huang, H. Yu, J. Chen, Z. Y. Lu, R. Yazami, H. H. Hng, *Adv. Mater*., 2014, **26**, 1296.
35 S-T. Myung, M. Kikuchi, C. S. Yoon, H. Yashiro, S-J. Kim,Y-K. Sun, B. Scrosati, *Energy Environ. Sci.,* 2013, **6**, 2609.
36 N. Kumagai, Y. Koishikawa, S. Komaba, N.Koshiba, *J. Electrochem. Soc.,* 1999, **146**, 3203.
37 X. Y. Wu, J. Miao, W. Z. Han, Y-S. Hu, D. F. Chen, J-S. Lee, J. Kim, L. Q. Chen, *Electrochem. Commun.,* 2012, **25**, 39.
38 H. S. Li, L. F. Shen, X. G. Zhang, P. Nie, L. Chen, K. Xu, *J. Electrochem. Soc.,* 2012, **159**, A426.
39 L. F. Shen, C. Z. Yuan, H. J. Luo, X. G. Zhang, K. Xu, Y. Y. Xia, *J. Mater. Chem.,* 2010, **20**, 6998.
40 H. Jiang, Y. Fu, Y. J. Hu, C. Y. Yan, L. Zhang, P. S. Lee, C. Z. Li, *Small,* 2014, **10**, 1096.
41 Y. L. Ding, X. B. Zhao, J. Xie, G. S. Cao, T. J. Zhu, H. M. Yu, C. Y. Sun, *J. Mater. Chem.,* 2011, **21**, 9475.
42 L. Yu, H. B. Wu, X. W. Lou, *Adv. Mater.,* 2013, **25**, 2296.
43 L. J. Xi, H. K. Wang, S. L. Yang, R. G. Ma, Z. G. Lu, C. W. Cao, K. L. Leung, J. Q. Deng, A. L. Rogach, C.Y. Chung, *J. Power Sources*, 2013, **242**, 222.
44 Y. H. Yin, J. J. Xu, Z. X. Cao, H. Y. Yue, S. T. Yang, *Mater. Lett.,* 2013, **108**, 21.
45 S. L. Chou, J. Z. Wang, H. K. Liu, S. X. Dou, *J. Phys. Chem. C,* 2011, **115**, 16220.
46 L. Chen, L. F. Shen, P. Nie, X. G. Zhang, H. S. Li, *Electrochim. Acta*, 2012, **62**, 408.